Journal of
Materials Chemistry A
Materials for energy and sustainability

This article can be cited before page numbers have been issued, to do this please use: X. Li, T. Wang, X. Tao, G. Qiu, C. Li and B. Li, *J. Mater. Chem. A*, 2020, DOI: 10.1039/D0TA05733A.

ROYAL SOCIETY
OF CHEMISTRY

rsc.li/materials-a

View Article Online
DOI: 10.1039/D0TA05733A

Interfacial Synergy of Pd Sites and Defective BiOBr for Promoting Solar-Driven Selective Oxidation of Toluene

Xiaoli Li [#,a], Ting Wang [#,a], Xueqin Tao [a], Ganhua Qiu [a], Can Li [b,*], Benxia Li [a,*]

[a] *Department of Chemistry, School of Science, Zhejiang Sci-Tech University, Hangzhou 310018, China*

b Institute of optoelectronic materials and devices, College of optical and electronic technology, China Jiliang University, Hangzhou 310018, China

*Corresponding author. Prof. Benxia Li, Email: libx@mail.ustc.edu.cn; Prof. Can Li, Email: Canli@cjlu.edu.cn

[#] X. L. Li and T. Wang contributed equally to this work.

View Article Online
DOI: 10.1039/D0TA05733A

ABSTRACT: Metal-modified semiconductors are being deemed as one kind of the most promising photocatalysts for various applications. Although great efforts have been devoted to developing a variety of metal-modified semiconductor photocatalysts, the exact functions of their interfaces in governing photocatalytic processes still remain elusive. Herein, the interfacial synergy of metal sites and defective semiconductor with oxygen vacancies (V_Os) is investigated toward the photocatalytic selective oxidation of toluene, by taking the Pd/BiOBr photocatalyst as an example. The presence of Pd induces to generate more V_Os on BiOBr surface due to the electronic interaction at Pd-BiOBr interface. The coexistence of Pd and V_O sites on BiOBr enables the favorable adsorption of O_2 and toluene molecules. The Pd-BiOBr interface governs the charge separation and prompts the activation of O_2 and toluene, leading to a 1.5-times activity of BiOBr-V_O for photocatalytic selective oxidation of toluene to benzaldehyde with a high selectivity (> 99%). Moreover, the typical influencing factors, such as illumination intensity and toluene concentration, are optimized to improve the photocatalytic efficiency. The active species and intermediates in the photocatalytic reaction are identified by a series of controlled experiments as well as in situ ESR measurements. Therefore, both experimental and theoretical results provide the direct evidence to understand the key roles of interfacial Pd and V_O sites in enhancing the photocatalysis toward selective oxidation of toluene.

Keywords: *metal-semiconductor interface; oxygen vacancy; synergetic effect; photocatalysis; selective oxidation.*

View Article Online
DOI: 10.1039/D0TA05733A

Introduction

The selective transformation of sp^3 C−H bonds in alkanes or aromatics for the production of value-added products has been always an attractive issue of great significance for both the studies in lab and the chemical productions.[1] Especially, the selective oxidation of the organic pollutant toluene to valuable benzaldehyde under mild and eco-friendly conditions is one of the most desirable reactions for fine chemicals and pharmaceuticals production.[2,3] The conversion of toluene to benzaldehyde in the present industrial processes is achieved mainly by chlorination of toluene and subsequent hydrolysis,[4] which is usually plagued by harsh reaction conditions, toxic acidic waste generation, and lower selectivity of benzaldehyde. Recently, the selective oxidation of toluene via the heterogeneous photocatalysis using molecular oxygen as an oxidant is attracting intensive interest,[5-8] because of its distinct advantages for solar energy utilization and high selectivity to the target products. Notwithstanding, the photocatalytic selective oxidation of toluene with O_2 to benzaldehyde is still a more challenging task, in comparison with the selective oxidation of active and expensive alcohol substrates,[9-11] due to the high bond dissociation energy of $C(sp^3)$−H bonds and the low adsorbability of toluene molecules.[12,13] Therefore, it is continuously desired to develop heterogeneous photocatalysts with high activity for the selective oxidation of toluene to benzaldehyde.

In photocatalytic reactions, the photoexcited electrons and holes are separated to drive reduction and oxidation, respectively. Engineering the adjacent active sites for

View Article Online
DOI: 10.1039/D0TA05733A

the respective reactions driven by electrons and holes could accelerate the reduction and oxidation occurring in series.[14] The photocatalytic selective oxidation of toluene to benzaldehyde using O_2 as an oxidant generally involves the electron-driven reduction of O_2 molecules and the hole-driven oxidation of $C(sp^3)-H$ bonds in toluene, where the reactive oxygen species (ROSs) generated from O_2 reduction can react rapidly with the hole-activated toluene intermediate to produce benzaldehyde.[5,15,16] Engineering the adjacent active sites for activating O_2 and toluene will be certainly of much help in accelerating the selective oxidation of toluene. Constructing the metal−oxide interfaces provides a new opportunity to tune different active sites and enable their synergetic effects based on the interfacial interaction.[17-19] Depositing metal nanoparticles (NPs) on oxide semiconductor is an effective strategy to improve the photocatalytic activity, because the metal NPs can not only act as electron traps to facilitate the interfacial charge separation and transfer,[20] but also offer the active sites for the adsorption and activation of substrate molecules.[21,22] In such heterostructure photocatalysts, the rational construction of heterogenous interfaces plays a critical role in determining the charge transfer efficiency and consequent reaction activity.[23,24] The metal-oxide interfacial interaction can induce the generation of a high concentration of oxygen vacancies (V_Os) at the interface, forming the adjacent metal-V_O dual active sites to promote synergistically the photocatalytic reactions.[25-27] Moreover, the introduction of V_O defects can further modulate the energy band structure and surface active sites to enhance the light absorption, charge mobility, and catalytic activity of the photocatalysts.[28-30] Therefore, constructing the metal-oxide

View Article Online
DOI: 10.1039/D0TA05733A

interfaces can achieve synchronously the multiple purposes of tuning energy band structure, inhibiting the electron-hole recombination and engineering active sites of photocatalysts. These advantages inspire that creating a metal/oxide photocatalyst with metal-V_O dual active sites at the interface holds great promise to enhance the efficiency of photocatalytic selective oxidation of toluene.

To confirm the above-mentioned opinions, bismuth oxybromide (BiOBr) was selected as a model of oxide semiconductor due to its suitable energy band levels, unique layered structure with alternatively arranged $[Bi_2O_2]^{2+}$ slabs and double Br^- slabs, as well as the special {001} facets being inclined to generate V_Os under mild conditions.[31,32] Besides, Pd NPs have been recognized as versatile catalysts in various organic oxidation reactions, because of their outstanding capability for O_2 activation to produce ROSs ($^1O_2$ and $\bullet O_2^-$).[33,34] Although a few previous investigations on the preparation of Pd/BiOBr photocatalysts and their applications in degradation of organic pollutants have been reported,[35-38] the exact functions and synergetic effects of different active sites at Pd-BiOBr interface for promoting the photocatalytic selective oxidation were seldom studied. This work focuses on constructing the Pd/BiOBr photocatalyst with metal-V_O dual active sites and revealing their synergy for photocatalytic selective oxidation of toluene to produce benzaldehyde. It is found that the Pd-BiOBr interfacial interaction not only stabilizes the small Pd NPs but also induces more V_Os on BiOBr surface. Both experimental results and theoretical calculations indicate that the hole-driven toluene oxidation at the Pd-BiOBr interface is easier to occur than that directly on the BiOBr surface without Pd NPs. Meanwhile,

View Article Online
DOI: 10.1039/D0TA05733A

the electrons trapped on Pd sites expedite the O_2 activation to afford sufficient ROSs. The coexistence of Pd and V_O sites at Pd-BiOBr interface obviously improves the efficiency of photocatalytic selective oxidation of toluene to benzaldehyde.

Experimental

Chemicals

Bismuth nitrate pentahydrate ($Bi(NO_3)_3 \cdot 5H_2O$), polyvinylpyrrolidone (PVP-K30), potassium bromide (KBr), ammonium tetrachloropalladate ($(NH_4)_2PdCl_4$), ethylene glycol (EG), mannitol, ammonium oxalate (AO), benzoquinone (BQ), isopropanol (IPA), potassium persulfate ($K_2S_2O_8$), β-carotene, catalase (≥ 200000 unit/g), superoxide dismutase (SOD, ≥ 1400 units/mg), 3,3',5,5'-tetramethylbenzidine (TMB), 5,5-dimethyl-pyrroline-N-oxide (DMPO) and 2,2,6,6-tetramethylpiperidine (TEMP) were purchased from Aladdin Biochemical Technology Co. Ltd. Toluene, p-chlorotoluene, p-bromotoluene, p-methyltoluene and p-methoxytoluene were purchased from Shanghai Macklin Biochemical Co. Ltd. All chemical regents were used without further purification.

Synthesis of BiOBr nanostructures

The nanosheet-assembled BiOBr nanostructures were synthesized by a solvothermal process. Typically, 1 mmol $Bi(NO_3)_3 \cdot 5H_2O$ and 1 mmol KBr were dissolved in 30 mL ethylene glycol in sequence to form a transparent solution. Then 0.2 g PVP and 0.05 g mannitol were dissolved in the solution. After 20 min stirring, the solution was transferred into a 50 mL solvothermal autoclave which was sealed and kept at 160 °C

View Article Online
DOI: 10.1039/D0TA05733A

for 8 h. After the reaction, the precipitate was collected by centrifugation, washed with deionized water and ethanol consecutively, and dried at 60 °C.

Preparation of Pd/BiOBr photocatalysts

The Pd/BiOBr photocatalysts were prepared by photodeposition of Pd NPs on the nanosheets-assembled BiOBr nanostructures. Typically, 20 mg BiOBr sample was dispersed in 10 ml deionized water by ultrasonic, and a certain volume of $(NH_4)_2PdCl_4$ aqueous solution (0.01 M) was injected into the BiOBr suspension. After stirred for 30 min in dark, the suspension was exposed to a LED irradiation (λ = 365 nm, optical power density = 2.04 mW/cm^2) for 10 min with continuously stirring. The final product was obtained by centrifugation, washing and drying in sequence.

Characterization

X-ray diffraction (XRD) analysis was performed on Shimadzu XRD-6000 diffractometer using a monochromatic Cu Kα radiation with a scan rate of 5°/min. Scanning electron microscope (SEM) images were recorded by a Zeiss Ultra 55 instrument with a 20 kV accelerating voltage. Transmission electron microscope (TEM) and high resolution TEM (HRTEM) images were taken on a Hitachi S4800 instrument. The specific surface areas and pore size distributions of the samples were calculated by Brunauer-Emmet-Teller (BET) and Barrett-Joyner-Halenda (BJH) models, respectively, on the basis of N_2 adsorption/desorption process performed on a Micromeritics ASAP 2020 instrument. X-ray photoelectron spectra (XPS) were detected by a thermal SCIENTIFIC ESCALAB 250Xi X-ray photoelectron spectrometer, and the binding energies were calibrated internally by the C 1s at 284.8

eV. UV–vis diffuse reflectance spectra (DRS) were recorded on a UV–vis spectrometer (UV-2600, Shimadzu, Japan) with $BaSO_4$ as the reference sample. The photoluminescence (PL) properties of the samples were analyzed by Edinburgh FL/FS900 spectrophotometer using the excitation of 250 nm wavelength. Time-resolved fluorescence decay spectra were acquired according to the time-dependent single photon counting method on the Edinburgh FS5 fluorescence spectrometer. The electron spin resonance (ESR) measurements were performed at room temperature on a Bruker model JEOL JES-FA200 spectrometer, with using the same quartz capillary tubes for all the sample testing. The photoelectrochemical properties of the materials were tested by a three-electrode system referring to our previous report.[39]

Photocatalytic tests

The photocatalytic reactions were performed under the irradiation of Xe lamp (PLS-SXE300, Beijing Perfectlight Technology Co. Ltd.). For a typical reaction, 5 mg photocatalyst, 0.05 mmol toluene and 2 mL acetonitrile were mixed in a transparent quartz test tube which has a diameter of 1.5 cm and a length of 12 cm. After the reaction suspension was bubbled with O_2 for 30 min, the test tube was sealed by a balloon full of O_2 (~1 atm) and then exposed to the irradiation. After 5 h of irradiation, the reaction solution was collected, centrifuged, and filtered through a syringe filter to remove photocatalyst particles. The filtrate was analyzed by a gas chromatograph (GC-2014C, Shimadzu) with a KB1701 capillary column and using bromobenzene as the internal standard, to determine the content of each product. The

View Article Online
DOI: 10.1039/D0TA05733A

conversion of toluene and the selectivity for producing benzaldehyde were calculated by Eqs. (1)-(2):

$$Conversion\ (\%) = \frac{\sum content\ (mmol)\ of\ each\ product\ analyzed\ by\ GC}{substrat\ (mmol)} \times 100\% \qquad (1)$$

$$Selectivity\ (\%) = \frac{content\ of\ corresponding\ product\ (mmol)}{\sum content\ (mmol)\ of\ each\ product} \times 100\% \qquad (2)$$

Identification of photocatalytic reactive species

The reactive species produced in the photocatalytic selective oxidation of toluene, such as carbon radical, $^1O_2$ and $\cdot O^{2-}$, were detected by ESR spectroscopy, in which DMPO was used to trap $\cdot O^{2-}$ and carbon radicals and TEMP was used to trap $^1O_2$. In addition, the reactive species were also identified by a series of controlled experiments with adding various scavengers into the photocatalytic reaction suspension to scavenge the corresponding reactive species. For example, ammonium oxalate, benzoquinone, isopropanol, $K_2S_2O_8$ and BHT were used as scavengers to trap holes (h^+), $\cdot O^{2-}$, hydroxyl radical ($\cdot OH$), electrons (e^-) and carbon radicals, respectively. TEMPO can scavenge almost all of the radicals.

Theoretical calculations

The surfaces of BiOBr-Vo (001) with and without Pd cluster were built, respectively, where the vacuum space along the z direction was set to be 20 Å. Then the O_2 and $C_6H_5CH_3$ molecules were adsorbed on the surfaces, respectively. The three atomic layers at bottom were fixed and the three atomic layers at top were relaxed adequately for all systems. The first principles calculations in the framework of density functional theory (DFT) were carried out based on the Cambridge Sequential Total Energy Package known as CASTEP. The exchange–correlation functional under the

View Article Online
DOI: 10.1039/D0TA05733A

generalized gradient approximation (GGA) with norm-conserving pseudopotentials and Perdew–Burke–Ernzerhof (PBE) functional was adopted to describe the electron–electron interaction. An energy cutoff of 750 eV was used and a k-point sampling set of 5×5×1 was tested to be converged. A force tolerance of 0.01 eV·$Å^{-1}$, energy tolerance of 5.0×10^{-7} eV per atom and maximum displacement of 5.0×10^{-4} Å were considered. The adsorption energy of O_2 and $C_6H_5CH_3$ molecules were calculated by Eq.(3),[40] where E_{*A}, E_* and E_A denote the energy of adsorbed system, clear surface, and adsorbate (A = O_2 or $C_6H_5CH_3$), respectively.

$$\Delta E_A = E_{*A} - E_* - E_A \qquad (3)$$

Results and discussion

Compositions and structures of BiOBr and Pd/BiOBr photocatalysts

The Pd/BiOBr heterostructure photocatalyst was prepared via a two-step process shown in Fig. 1a, where the BiOBr flower-like nanostructures were synthesized through a solvothermal reaction and then modified by Pd NPs via LED-light induced deposition. In the synthesis, the addition of mannitol has distinct influence on the sizes and surface structures of BiOBr nanostructures, because the polyhydroxyl characteristics of mannitol makes it a good multi-dentate ligand strongly interacting with Bi^{3+} ions.[41,42] The BiOBr flower-like spheres synthesized with mannitol have the relatively more uniform diameters of ~ 600 nm and the nanosheets for building the flower-like spheres show the less average thickness about 15 nm (Fig. S1a), compared with the BiOBr(no mannitol) sample synthesized in the absence of mannitol (Fig. S1b). XRD patterns (Fig. S1c) of both the BiOBr samples are well matched with that

View Article Online
DOI: 10.1039/D0TA05733A

of tetragonal BiOBr (JCPDS No. 9-393), while the XRD peaks of BiOBr sample are obviously wider than those of BiOBr(no mannitol), confirming the smaller crystalline size of BiOBr sample. Moreover, ESR spectra (Fig. S1d) indicate that the addition of mannitol in the synthesis can induce the generation of more V_O defects in BiOBr. Therefore, the BiOBr flower-like nanostructures synthesized in the presence of mannitol are used to prepare the Pd/BiOBr photocatalysts. After photodepositing Pd NPs, the crystalline phase of BiOBr remains unchanged in the Pd(*x*)/BiOBr samples with various theoretical Pd contents (*x*) (Fig. 1b and Fig. S2), whereas the diffraction peaks of Pd are unobservable due to the small sizes and high dispersity of Pd NPs. Fig. 1c-f display SEM and TEM images of the Pd/BiOBr sample with a theoretical Pd content of 1.0 wt% which was optimized to possess the best photocatalytic activity, and the Pd/BiOBr sample mentioned below is this sample unless otherwise specified. The Pd/BiOBr heterostructures maintain well the flower-like morphology of BiOBr nanostructures. HRTEM image (Fig. 1d) of Pd/BiOBr sample presents two sets of lattice structures, and the interplanar spacings of 2.74 and 2.25 Å are corresponding to those of (110) plane in tetragonal BiOBr and (111) plane in cubic Pd, respectively. The sizes of Pd NPs in the Pd/BiOBr sample are estimated according to TEM observation (Fig. 1e), which indicates that the Pd NPs with a small average size of ~4.0 nm are highly dispersed on the nanosheets of BiOBr nanostructures. Moreover, the uniform distribution of Pd element in the Pd/BiOBr sample is further confirmed by SEM-associated EDX element mapping (Fig. 1f and g). These results demonstrate that the small Pd NPs have been evenly anchored on the nanosheets of BiOBr

View Article Online
DOI: 10.1039/D0TA05733A

nanostructures. The surface structures of BiOBr and Pd/BiOBr samples are determined by BET and BJH models, respectively, on the basis of N_2 adsorption/desorption process (Fig. S3). Both the samples exhibit the similar adsorption/desorption isotherms and pore size distribution profiles. The BET specific surface areas of BiOBr and Pd/BiOBr are 13.7 and 11.5 $m^2 \cdot g^{-1}$, respectively, and their average pore sizes are 29.9 and 28.3 nm (Table S1), indicating that Pd loading has little influence on the surface area and pore size distribution of BiOBr nanostructures.

XPS spectra (Fig. 2a-e) provide further information about the surface element compositions and their chemical states of BiOBr before and after loading Pd NPs. Both the XPS survey spectra (Fig. 2a) show notable signals of Bi, O, Br, and C elements, whereas the signal of Pd is hardly observed in the survey spectrum of Pd/BiOBr sample due to the low Pd content. The high-resolution Pd 3d spectrum (Fig. 2b) of Pd/BiOBr sample can be fitted with two doublets of Pd $3d_{5/2}$ and Pd $3d_{3/2}$ from spin-orbit splitting. The predominant doublet at 335.5-340.5 eV is characteristic of metallic Pd^0, and the other doublet with lower intensity at higher binding energies of 337.0-342.5 eV is corresponding to the oxidized state of Pd^{2+}.[43] The presence of a little Pd^{2+} can be ascribed to the electron transfer from surface Pd atoms to the chemisorbed oxygen.[44] The XPS peaks of Bi 4f (Fig. 2c) and Br 3d (Fig. 2d) in both BiOBr and Pd/BiOBr samples are assigned to Bi^{3+} cations and Br^- anions, respectively,[45] whereas the peaks of Pd/BiOBr sample shift towards the higher binding energies with respect to the ones of BiOBr sample, suggesting that the electron transfer occurs from BiOBr to Pd at Pd-BiOBr interface due to a large

View Article Online
DOI: 10.1039/D0TA05733A

difference in the work functions of Pd (5.11 eV) and BiOBr (2.93 eV).[44,46,47] The O 1s spectra (Fig. 2e) of both BiOBr and Pd/BiOBr samples are fitted with three peaks at 529.8/530.1, 531.2/531.5, and 531.9/532.2 eV, respectively, corresponding to the lattice oxygen of BiOBr, the adsorbed oxygen at V_O sites and the hydroxyl groups.[30] The binding energies of O 1s in Pd/BiOBr sample also present positive shifts in comparison with BiOBr sample, which can also be ascribed to the intimate interfacial integration and interaction between Pd and BiOBr in forming heterostructures.[48] The adsorbed oxygen species at V_O sites in Pd/BiOBr sample account for a higher proportion (30.5%) of the O 1s peak, compared with that (24.4%) for BiOBr sample, suggesting a higher V_O concentration induced by Pd loading. In ESR spectra (Fig. 2f), the characteristic V_O signal with a g factor of 2.0 is observed for both BiOBr and Pd/BiOBr samples. Moreover, the higher signal intensity indicates the increase in V_O concentration of Pd/BiOBr sample compared with that of pure BiOBr, meaning that Pd NPs induces the generation of more V_O defects in BiOBr due to the interfacial interaction between Pd and BiOBr. The interfacial interaction stabilizes small Pd NPs and V_Os, which will be beneficial to the excitation, migration and separation of photogenerated electrons and holes.

Photoabsorption and photoexcited charge separation

The photoabsorption of BiOBr and Pd/BiOBr samples are analyzed by UV-vis DRS spectroscopy, and the Kubelka-Munk transformed absorption spectra are shown in Fig. 3a. The BiOBr sample shows a strong absorption in UV region ($\lambda \leq 400$ nm) and a weak tailing absorption in visible region due to the presence of surface defects.[49] For

View Article Online
DOI: 10.1039/D0TA05733A

Pd/BiOBr sample, the optical absorption in visible region is enhanced by introducing Pd NPs, and the absorption edge of BiOBr shifts a little to longer wavelength. The room-temperature steady-state photoluminescence (PL) spectra of both BiOBr and Pd/BiOBr samples are employed to evaluate the photoexcited electron-hole separation efficiencies in the photocatalysts (Fig. 3b). Under an excitation wavelength of 250 nm, BiOBr sample shows a very strong emission band around 390 nm derived from the indirect radiative recombination of photoexcited electrons and holes.[50] In comparison, the Pd/BiOBr heterostructures exhibit a remarkably quenched fluorescence emission, suggesting that the recombination of photoexcited charge carriers is suppressed in the Pd/BiOBr sample. The time-resolved photoluminescence (TRPL) analysis is further used to determine the photoexcited charge carrier dynamics of BiOBr and Pd/BiOBr samples. Both the TRPL decay curves (Fig. 3c) can be fitted by the following biexponential function:

$$\mathrm{I}_{(t)} = A_1 \exp(-t/\tau_1) + A_2 \exp(-t/\tau_2) \tag{4}$$

where τ_i and A_i denote the fluorescent lifetime and its weighing factor, respectively.[51,52] The average fluorescent lifetimes (τ_m) of BiOBr and Pd/BiOBr are 0.84 and 0.58 ns (Table S2), respectively. In the present case, the electron transfer from BiOBr to Pd NPs guarantees the efficient separation of photoexcited electrons and holes, thus shortening the fluorescent lifetime of Pd/BiOBr heterostructures.[51,52] To further demonstrate the photoexcited charge separation efficiencies and electron transfer abilities of BiOBr and Pd/BiOBr photocatalysts, their photocurrent responses and electrochemical impedance spectroscopy (EIS) Nyquist plots were measured

View Article Online
DOI: 10.1039/D0TA05733A

under the Xe lamp irradiation. The higher photocurrent intensity (Fig. 3d) of Pd/BiOBr suggests the more efficient separation of photoexcited holes and electrons.[53] The EIS Nyquist plot (Fig. 3e) of Pd/BiOBr shows a smaller arc radius than that of BiOBr sample, indicating that the introduction of Pd NPs can promote the charge transfer.[54] Fig. 3f shows the Mott−Schottky (M-S) plots of the BiOBr and Pd/BiOBr photoelectrodes, where the positive slopes of the linear regions indicate the characteristic of n-type semiconductor for BiOBr nanostructures before and after loading Pd NPs.[55,56] Moreover, the slopes of the linear regions is inversely proportional to the charge carrier density (N_D) of the photoelectrode.[57,58] The declined slope in the M–S plot of Pd/BiOBr sample, compared with that of BiOBr sample, reveals the higher charge carrier density in Pd/BiOBr.

DFT calculations were further performed to elucidate the electronic interaction at Pd–BiOBr interface. The optimized structures of BiOBr-V_O (001) without and with Pd cluster are shown in Fig. S4. The BiOBr-V_O (001) surface was built by cutting the crystal lattice along (001) plane with Bi atomic layer as the terminated surface, with one V_O site being introduced. The introduction of V_O site leads to local distortion of BiOBr (001) surface. The BiOBr-V_O (001) with Pd cluster was built by anchoring a Pd_{12} cluster on the BiOBr-V_O (001) surface. Fig. 4a shows the partial density of states (PDOS) of two systems. The conduction band (CB) of BiOBr-V_O (001) is predominated by Bi 6p orbitals, while the valence band (VB) is mainly occupied by Br 4p orbitals hybridized with the low-density O 2p state.[31,59] In contrast, for BiOBr-V_O (001) with Pd cluster, Pd 4d electron state contributes significantly to

View Article Online
DOI: 10.1039/D0TA05733A

enhancing the charge density above the valence band maximum (VBM) of BiOBr, which is greatly beneficial to the generation and migration of photoinduced electrons. The charge density difference (Fig. 4b) of BiOBr-V_O (001) with Pd cluster provides further insight into the charge density variation of the Pd-BiOBr interface, indicating that the Pd sites at the interface are the electron accumulation area. This confirms the obvious electronic interaction at the Pd-BiOBr interface and electrons are trapped by the interfacial Pd sites. At the Pd-BiOBr interface, electrons transfer from BiOBr to Pd for aligning the Fermi levels, due to the larger work function (5.11 eV) of Pd than that (2.93 eV) of BiOBr,[46,47] forming the Schottky barrier at the interface (Fig. 4c).[60] The Schottky barrier can prevent the recombination of photoinduced electron–hole pairs. The interfacial electron transfer from BiOBr to Pd leaves positive charges on BiOBr, which has been verified by XPS spectra described above where the electronic binding energies of BiOBr in Pd/BiOBr sample shift positively, compared with those of BiOBr without Pd NPs. In consequence, the electrons are trapped by the Pd sites in the vicinity of the interface; meanwhile the holes migrate toward the interface around the Pd NPs for the charge balance, as shown in Fig. 4d. The resultant charge-separated states at the Pd-BiOBr interface (electrons in Pd sites and holes in BiOBr) are highly conducive to the subsequent chemical transformations consisting of reduction and oxidation steps.

Photocatalytic performance for selective oxidation of toluene

Based on all the analysis results above, the unique interface of Pd/BiOBr heterostructures predicts its superior photocatalysis for selective oxidation of toluene

View Article Online
DOI: 10.1039/D0TA05733A

with O_2 as an oxidant (Fig. 5a). The photocatalytic performance of BiOBr and Pd/BiOBr with different Pd loadings was screened by the selective oxidation of toluene (0.05 mmol toluene in 2 mL acetonitrile) under UV-vis irradiation with an optical power density of 200 mW·cm^{-2}. As shown in Fig. 5b and Table S3, these photocatalysts exhibit high selectivity (> 99%) for producing benzaldehyde from toluene oxidation. The BiOBr nanostructures without Pd NPs show the mediocre photocatalytic activity with a toluene conversion rate of 317.8 μmol·g_{cat}^{-1}·h^{-1}. After loading Pd NPs, the selective oxidation of toluene is further improved. When the Pd(*x*)/BiOBr samples with different Pd mass fractions (*x* wt.%) are used as photocatalysts, the toluene conversion rate presents a peak-like variation with the Pd loading contents and achieves a maximum value of 476.8 μmol·g_{cat}^{-1}·h^{-1} over the Pd(*1.0*)/BiOBr photocatalyst. The Pd(*1.5*)/BiOBr and Pd(*2.0*)/BiOBr samples exhibit the gradually depressed photocatalytic activities, which can be ascribed to the formation of larger Pd NPs (Fig. S5) with the reduced active sites. The results indicate that the dispersion of Pd NPs have an obvious effect on the photocatalytic selective oxidation of toluene. In addition, the BiOBr(water) sample consisting of large nanosheets (Fig. S6) is synthesized by a hydrothermal process in the absence of any organic additive. The Pd/BiOBr(water) and Pd/BiOBr(no mannitol) samples with each theoretical Pd content of 1.0 wt% are also prepared by the same photodeposition process as that for the preparation of Pd/BiOBr photocatalyst. By comparison, the activities of various photocatalysts in an increasing order are: BiOBr(water) < BiOBr(no mannitol) < Pd/BiOBr(water) ≈ BiOBr < Pd/BiOBr(no mannitol) <

View Article Online
DOI: 10.1039/D0TA05733A

Pd/BiOBr, as shown in Fig. S7 and Table S3. The results indicate that the critical factors influencing the photocatalytic activities toward selective oxidation of toluene are Pd loading as well as the V_O concentration in BiOBr nanostructures. The flower-like nanostructures of BiOBr synthesized by the solvothermal process with mannitol have the highest V_O concentration, compared with BiOBr(water) and BiOBr(no mannitol). As a result, the Pd/BiOBr photocatalyst exhibits the best photocatalytic performance due to the synergy of Pd and V_O sites at the interface of Pd/BiOBr photocatalyst. Furthermore, as shown in Fig. 5c, the Au/BiOBr photocatalyst exhibits a lower toluene conversion (331.9 $\mu mol \cdot g_{cat}^{-1} \cdot h^{-1}$) than that from the Pd/BiOBr photocatalyst (476.8 $\mu mol \cdot g_{cat}^{-1} \cdot h^{-1}$), confirming the favorable function of Pd NPs in improving the photocatalytic activity toward selective oxidation of toluene to benzaldehyde. This should be attributed to the fact that oxygen molecules are more easily activated on the surface of Pd NPs than Au ones.[61] The calcinations of BiOBr and Pd/BiOBr samples at 350 °C in air lead to the remarkable drops in their photocatalytic activities because V_Os in the samples can be filled by oxygen from air during the calcination process, which further testify that the integration of well-dispersive Pd sites and abundant V_Os in Pd/BiOBr heterostructures is crucial for promoting the photocatalytic selective oxidation of toluene. The temperature of the photocatalytic suspension with Pd/BiOBr is measured to be 45 ℃ after being exposed to the irradiation for 5 h. Whereas, the toluene conversion cannot occur over the Pd/BiOBr catalyst at 45 ℃ in dark even after heating for 5 h (Fig. 5c), excluding the thermal effect on the photocatalytic selective oxidation of toluene over

View Article Online
DOI: 10.1039/D0TA05733A

Pd/BiOBr under the present conditions. In addition, the toluene conversion hardly proceeds when the photocatalytic reaction is performed in high purity N_2 atmosphere, confirming the necessity of O_2 in photocatalytic selective oxidation of toluene.

The light intensity, which influences the photoexcitation of photocatalyst, also affects the photocatalytic efficiency of toluene oxidation. The performance of the optimal Pd/BiOBr photocatalyst is further probed under the UV-visible light with varied optical power densities, as shown in Fig. 5d and Table S4. The conversion rate of toluene to benzaldehyde is enhanced from 333.8 to 476.8 $\mu mol \cdot g_{cat}^{-1} \cdot h^{-1}$ as the optical power density of irradiation increases from 100 to 200 $mW \cdot cm^{-2}$. The stronger irradiation induces the generation of more electrons and holes, enhancing the photocatalytic efficiency of selective toluene oxidation. However, the photocatalytic conversion of toluene over Pd/BiOBr declines when the optical power density is further increased to 300 $mW \cdot cm^{-2}$. It has been reported that the plasmonic effect of Pd nanocrystals could generate a reverse flow of electrons from Pd to the CB of adjacent semiconductor under strong illumination, which could lower the electron density of Pd surface in opposition to the function of the Schottky junction.[33] Therefore, the transfer of electrons from BiOBr to Pd dominates when the irradiation is relatively weak (< 200 $mW \cdot cm^{-2}$), where the charge densities on Pd and BiOBr increase with the enhancive incident illumination, thus enhancing the photocatalytic efficiency; whereas, the efficiency is lowered by the plasmonic effect of Pd NPs under the stronger illumination (> 200 $mW \cdot cm^{-2}$). Fig. 5e and Table S5 show the effect of the toluene dosage on its oxidation conversion rate over the Pd/BiOBr photocatalyst. The

DOI: 10.1039/D0TA05733A

higher toluene loading in the photocatalytic system increases the possibility of toluene adsorption on the active sites of photocatalyst, resulting in a higher conversion rate of toluene. When 9.4 mmol of toluene is added initially, the conversion rate achieves as high as 6022.5 μmol·g_{cat}^{-1}·h^{-1}.

Subsequently, the Pd/BiOBr photocatalyst was further used toward the selective oxidation of several toluene derivatives with different substituents under the same conditions (UV−visible irradiation of 200 mW·cm^{-2}, 0.05 μmol toluene in 2 mL acetonitrile). The results (Fig. 6a and Table S6) indicate that the selective oxidation of toluene derivatives into the aromatic aldehydes can also achieve the relatively high conversion rates (320.6−549.5μmol·g_{cat}^{-1}·h^{-1}) and excellent selectivity (> 99%) over the Pd/BiOBr photocatalyst. The substrates with electron-donating *para* substituents (−CH_3, −OCH_3) exhibit higher reactivity than the ones with electron-withdrawing *para* substituents (−F, −Cl), because the electron-donating groups on benzene ring facilitate the h^+-driven C(sp^3)−H oxidation.[6,62,63] The recyclability of the Pd/BiOBr photocatalyst was examined by the selective oxidation of toluene with 5 h irradiation for each cycle (Fig. 6b and Table S7). After five photocatalytic cycles, only a slight decrease in the toluene conversion rate is observed. Both the excellent activity and the high selectivity are well maintained after 25 h of the photocatalytic reaction. XRD, TEM and XPS analyses on the recycled Pd/BiOBr photocatalyst (Figs. 6c-f) demonstrate that the crystalline phase, microstructures and valence states of typical elements in the recycled Pd/BiOBr photocatalyst remain unchanged, verifying the high stability of Pd/BiOBr photocatalyst for a long-term photocatalytic reaction.

DOI: 10.1039/D0TA05733A

Insight into the photocatalytic mechanism

To acquire more insight into the photocatalytic mechanism of selective toluene oxidation on the Pd/BiOBr photocatalyst, the contributions of various active species to this reaction were investigated by the controlled experiments carried out in the presence of the radical scavengers. As displayed in Fig. 7a, the addition of isopropanol (IPA) acting as a hydroxyl radical (•OH) scavenger results in only a slight decrease in the toluene conversion rate, indicating that •OH radical is scarcely involved in the oxidation of toluene. In contrast, the conversion rate of toluene was extremely reduced by adding ammonium oxalate (AO) for eliminating holes (h^+) or butylated hydroxytoluene (BHT) for clearing off carbon-centered radicals which are generated usually from the hole-activated organic substrates.[5,64] In addition, the addition of *p*-benzoquinone (*p*-BQ) for clearing off superoxide radical ($•O_2^-$) also causes a remarkable declination in the conversion rate of toluene, suggesting the considerable contribution of $•O_2^-$ in this reaction. When tetra-methylpiperidine N-oxide (TEMPO) is introduced to quench all the radicals in the reaction system, the toluene oxidation is almost completely suppressed, which confirms that the photocatalytic selective oxidation of toluene undergoes a radical-initiated reaction pathway.[16,65] These results demonstrate that h^+, carbon-centered and $•O_2^-$ radicals dominate the photocatalytic process over Pd/BiOBr catalyst for selective oxidation of toluene. The active radicals generated in the photocatalytic reaction of toluene oxidation over BiOBr and Pd/BiOBr photocatalysts are further identified and compared by in situ ESR detection (Fig. 7b), respectively. The ESR signal is hardly observed in the reaction solution with whether BiOBr or Pd/BiOBr in dark. Under the irradiation, distinct peaks emerge in both the reaction systems, where the sextet peaks (★) are assigned to DMPO-carbon-centered radicals and the quartet peaks (♦) belong to DMPO-$\bullet O_2^-$ species.[64,66] Obviously, the signals of active radicals generated from Pd/BiOBr photocatalyst is more conspicuous than those from BiOBr, confirming the enhanced photocatalysis of Pd/BiOBr.

The activation of molecular oxygen usually plays a crucial role in the selective oxidation of organics with O_2 as an oxidant.[67] The ROSs stemmed from O_2 activation, generally including superoxide radical ($\cdot O_2^-$) and singlet oxygen ($^1O_2$), can react rapidly with the pre-adsorbed organic molecules or the organic intermediates to accomplish the oxidation reactions.[68,69] Therefore, the photocatalytic O_2 activation ability of Pd/BiOBr catalyst and the photogenerated ROSs were probed by TMB oxidation, on the basis of monitoring the absorbance evolution at 370 nm of TMB solution along the irradiation time (Figs. S8-10 and Fig. 7c).[70-72] The time-dependent absorption intensity of 370 nm peak from TMB solution without scavenger (Fig. S8 and Fig. 7c) indicates the superior O_2 activation ability of Pd/BiOBr than that of pure BiOBr. In addition, a series of controlled experiments in regard to TMB oxidation were performed by adding various scavengers in the solution, such as superoxide dismutase (SOD, quenching $\cdot O_2$), carotene (quenching $^1O_2$) mannitol (quenching $\cdot OH$), and catalase (quenching H_2O_2), respectively (Fig. 7c and Figs. S9-10), which can further distinguish the photoinduced ROSs involved in TMB oxidation. For BiOBr, TMB oxidation is mainly depressed by SOD but little affected by other scavengers, reflecting that $\cdot O_2^-$ radical is the major ROS generated from BiOBr. For Pd/BiOBr, TMB oxidation can be remarkably suppressed by adding SOD or carotene, suggesting that both $\cdot O_2^-$ and $^1O_2$ coexist as the major ROSs. Furthermore, the in situ ESR detection with using TEMP as a radical-trapping agent provides more direct evidence for the photogeneration of $^1O_2$ during photocatalytic toluene oxidation. As shown in Fig. 7d, the 1:1:1 triplet signal is characteristic of 2,2,6,6-Tetramethylpiperidine-N-oxyl (TEMPO), indicating the generation of $^1O_2$. In a sharp contrast, the triple-signal intensity is remarkably enhanced in the presence of Pd/BiOBr, suggesting the abundence of $^1O_2$ yield. According to the above results, the Pd/BiOBr photocatalyst possesses the higher ability for activating toluene and O_2 molecules, thus producing more carbon-centered radical and ROSs ($\cdot O_2^-$ and $^1O_2$), which contribute together to promoting the selective oxidation of toluene to benzaldehyde.

DFT calculations are performed to further reveal the active sites for substrate activation on the photocatalysts. The optimized configurations and adsorption energies of O_2 and toluene adsorbed onto V_O in BiOBr-V_O surface and different Pd sites in Pd/BiOBr-V_O surface are displayed in Fig. 8 and Table S8. By contrast, the Pd/BiOBr-V_O surface shows stronger interactions with O_2 and toluene molecules. In the Pd/BiOBr-V_O surface, the interfacial Pd site (labeled as Site 1) affords the most negative adsorption energy of -4.72 eV for toluene, due to the electron donation effect of the aryl ring in toluene to the Pd surface through the π-bond interaction.[44,73] This preferential adsorption configuration of toluene on the interfacial Pd site can keep the

View Article Online
DOI: 10.1039/D0TA05733A

methyl group close to the h^+-rich BiOBr surface, thus beneficial to the h^+-driven activation of C(sp^3)-H bonds. Moreover, the Pd sites show much stronger chemical interactions with O_2 than that of the BiOBr-V_O surface, where O_2 molecules can be adsorbed onto either interfacial or top Pd sites of Pd/BiOBr-V_O. As demonstrated above, both $\cdot O_2^-$ and $^1O_2$ are produced predominately in the photocatalytic reaction system with Pd/BiOBr. It is reasonable to consider that the two adsorption modes of O_2 on interfacial Pd site and top Pd site exist simultaneously, which induce the simultaneous generation of $\cdot O_2^-$ and $^1O_2$ through the transfer of electron and energy, respectively.[33] As a typical charge carrier process, the photocatalytic $\cdot O_2^-$ generation is generally determined by the concentration and transfer of surface free electrons.[71] The interfacial Pd site with higher electron density, as illustrated in Fig. 4d, is able to highly activate O_2 to $\bullet O_2^-$ via electron transfer. Besides, Pd NPs can also promote the generation of $^1O_2$ by inducing the spin-flip process in O_2 molecules.[33,69,74] The calculated results prove that the presence of Pd NPs enables the strong chemical adsorption of toluene and O_2 molecules on the photocatalyst, ensuring the efficient electron exchange and energy transfer between reactants and Pd/BiOBr photocatalyst.

Based on the experimental and calculation studies above, the photocatalytic mechanism of the selective toluene oxidation to benzaldehyde over the Pd/BiOBr photocatalyst is illustrated in Fig. 9. Upon the photo-excitation, the electrons and holes are generated and separated as the above descriptions, where the electrons are located at the interfacial Pd sites and the holes gather in the vicinity of the Pd NPs for the charge balance. The chemisorbed O_2 molecules are activated to generate $\cdot O_2^-$ and

View Article Online
DOI: 10.1039/D0TA05733A

$^1O_2$ at different Pd sites through the transfer of electron and energy, respectively. Meanwhile, the C(sp^3)-H bond of toluene are oxidized by holes to produce the benzyl radical. Subsequently, the generated ROSs ($\cdot O_2^-$ and $^1O_2$) react with the activated benzyl intermediates, to produce benzaldehyde and H_2O.[5,75] The Pd/BiOBr photocatalyst has been proved to possess a great superiority in the generation and separation of photoinduced electrons and holes due to the Schottky barrier at Pd-BiOBr interface, which facilitates the electron-driven activation of molecular O_2 and the hole-driven activation of C(sp^3)-H bonds in toluene. Moreover, the Pd NPs and defective BiOBr surface provide more active sites for the catalytic reactions, synergistically improving the reactivity and selectivity of photocatalytic selective oxidation of toluene to benzaldehyde.

Conclusions

The Pd/BiOBr photocatalyst, prepared by photodepositing Pd NPs on the V_O-rich BiOBr flower-like nanostructures, is taken as a model to study the synergetic effect of metal site and defective semiconductor at the interface for promoting the photocatalytic selective oxidation of toluene. The anchoring of Pd NPs can induce the generation of more V_Os on BiOBr surface owing to the electronic interaction between Pd and BiOBr, while the interfacial interaction stabilizes small Pd NPs and abundant V_Os. DFT calculations indicate that the presence of both Pd NPs and V_O on BiOBr surface enables the favorable adsorption of O_2 and toluene. Furthermore, the separated charge carriers at the Pd-BiOBr interface greatly promote the electron-driven activation of O_2 molecules and the hole-driven activation of C(sp^3)-H bonds in toluene, respectively. Both the experimental results and theoretical calculations substantiate that the toluene oxidation at the Pd–BiOBr interface is easier to occur than that directly on BiOBr surface, and the electrons gathered on Pd sites expedite the O_2 activation to afford sufficient ROSs ($\cdot O_2^-$ and $^1O_2$). The photocatalytic efficiency is optimized to achieve a considerable toluene conversion rate of 6022.5 $\mu mol \cdot g_{cat}^{-1} \cdot h^{-1}$. The active species and intermediates in the photocatalytic reaction are identified by a series of controlled experiments as well as in situ ESR measurements. Therefore, the synergetic effect of Pd NPs and V_O defects at the interface of Pd/BiOBr photocatalyst improves the performance toward photocatalytic selective oxidation of toluene to benzaldehyde. This study offers insight into the interfacial synergy of metal sites and V_O-rich oxide semiconductors for promoting photocatalytic selective oxidation reactions and is expected to guide future structural design and modulation of photocatalysts.

Conflicts of interest

There are no conflicts to declare.

Acknowledgments

This work was supported by the National Natural Science Foundation of China (21471004), the Natural Science Foundation of Zhejiang Province of China (LY19B010005 and LY18E020007), the Fundamental Research Funds of Zhejiang Sci-Tech University (2020Y003) and the Science Foundation of Zhejiang Sci-Tech

View Article Online
DOI: 10.1039/D0TA05733A

University (17062002-Y).

Notes and references

1 C. Coperet, *Chem. Rev.,* 2010, **110**, 656-680.

2 L. Kesavan, R. Tiruvalam, M. H. A. Rahim, M. I. bin Saiman, D. I. Enache, R. L. Jenkins, N. Dimitratos, J. A. Lopez-Sanchez, S. H. Taylor, D. W. Knight, C. J. Kiely and G. J. Hutchings, *Science*, 2011, **331**, 195-199.

3 D. D. Mal, S. Khilari and D. Pradhan, *Green Chem*., 2018, **20**, 2279-2289.

4 J. A. B. Satrio and L. K. Doraiswamy, *Chem. Eng. J*., 2001, **82**, 43-56.

5 X. Cao, Z. Chen, R. Lin, W. C. Cheong, S. Liu, J. Zhang, Q. Peng, C. Chen, T. Han, X. Tong, Y. Wang, R. Shen, W. Zhu, D. Wang and Y. Li, *Nat. Catal*., 2018, **1**, 704-710.

6 L. N. Song, F. Ding, Y. K. Yang, D. Ding, L. Chen, C. T. Au and S. F. Yin, *ACS Sustain. Chem. Eng*., 2018, **6**, 17044-17050.

7 J. He, L. Chen, D. Ding, Y. K. Yang, C. T. Au and S. F. Yin, *Appl. Catal. B: Environ*., 2018, **233**, 243-249.

8 W. Yang, B. Ling, B. Hu, H. Yin, J. Mao and P. J. Walsh, *Angew. Chem. Int. Ed*., 2020, **59**, 161-166.

9 B. Li, L. Shao, R. Wang, X. Dong, F. Zhao, P. Gao and Z. Li, *J. Mater. Chem. A*, 2018, **6**, 6344-6355.

10 L. Chen, J. Tang, L. N. Song, P. Chen, J. He, C. T. Au and S. F. Yin, *Appl. Catal. B: Environ*., 2019, **242**, 379-388.

View Article Online
DOI: 10.1039/D0TA05733A

11 X. Yang, S. Zhang, H. Tao, X. Yan, Y. Tan, Y. Zhang, S. Gao and R. Cao, *J. Mater. Chem. A*, 2020, **8**, 6854-6862.

12 H. Sterckx, B.Morel and B. U. W. Maes, *Angew. Chem. Int. Ed.*, 2019, **58**, 7946-7970.

13 Y. Dai, C. Poidevin, C. Ochoa-Hernández, A. A. Auer and H. Tüysüz, *Angew. Chem. Int. Ed.*, 2020, **59**, 5788-5796.

14 Y. Zhou, Z. Zhang, Z. Fang, M. Qiu, L. Ling, J. Long, L. Chen, Y. Tong, W. Su, Y. Zhang, J. C. S. Wu, J. M. Basset, X. Wang and G. Yu, *Proc. Natl. Acad. Sci. U. S. A.*, 2019, **116**, 10232-10237.

15 L. N. Song, L. Chen, J. He, P. Chen, H. K. Zeng, C. T. Au and S. F. Yin, *Chem. Commun.*, 2017, **53**, 6480-6483.

16 F. Liu, C. X. Xiao, L. H. Meng, L. Chen, Q. Zhang, J. B. Liu, S. Shen, J. K. Guo, C. T. Au and S. F. Yin, *ACS Sustain. Chem. Eng.*, 2020, **8**, 1302-1310.

17 X. Li, G. Liu, D. Xu, X. Hong and S. C. Edman Tsang, *J. Mater. Chem. A*, 2019, **7**, 23878-23885.

18 T. Gan, X. Chu, H. Qi, W. Zhang, Y. Zou, W. Yan and G. Liu, *Appl. Catal. B: Environ.*, 2019, **257**, 117943.

19 W. Huang, Q. Liu, Z. Zhou, Y. Li, Y. Ling, Y. Wang, Y. Tu, B. Wang, X. Zhou, D. Deng, B. Yang, Y. Yang, Z. Liu, X. Bao and F. Yang, *Nat. Commun.*, 2020, **11**, 2312.

20 H. Song, X. Meng, S. Wang, W. Zhou, X. Wang, T. Kako and J. Ye, *J. Am. Chem. Soc.*, 2019, **141**, 20507-20515.

21 L. Y. Lin, S. Kavadiya, X. He, W. N. Wang, B. B. Karakocak, Y. C. Lin, M. Y. Berezin and P. Biswas, *Chem. Eng. J.*, 2020, **389**, 123450.

22 S. Wu, X. Tan, J. Lei, H. Chen, L. Wang and J. Zhang, *J. Am. Chem. Soc.*, 2019, **141**, 6592-6600.

23 Z. Zhang and J. T. Yates, *Chem. Rev.*, 2012, **112**, 5520-5551.

24 S. Mo, Q. Zhang, M. Zhang, Q. Zhang, J. Li, M. Fu, J. Wu, P. Chen and D. Ye, *Nanoscale Horiz.*, 2019, **4**, 1425-1433.

25 M. Wang, M. Shen, X. Jin, J. Tian, M. Li, Y. Zhou, L. Zhang, Y. Li and J. Shi, *ACS Catal.*, 2019, **9**, 4573-4581.

26 M. Xiao, L. Zhang, B. Luo, M. Lyu, Z. Wang, H. Huang, S. Wang, A. Du and L. Wang, *Angew. Chem. Int. Ed.*, 2020, **59**, 7230-7234.

27 Y. Chen, S. Ji, W. Sun, Y. Lei, Q. Wang, A. Li, W. Chen, G. Zhou, Z. Zhang, Y. Wang, L. Zheng, Q. Zhang, L. Gu, X. Han, D. Wang and Y. Li, *Angew. Chem. Int. Ed.*, 2020, **59**, 1295-1301.

28 D. Cui, L. Wang, K. Xu, L. Ren, L. Wang, Y. Yu, Y. Du and W. Hao, *J. Mater. Chem. A*, 2018, **6**, 2193-2199.

29 X. Tong, X. Cao, T. Han, W. C. Cheong, R. Lin, Z. Chen, D. Wang, C. Chen, Q. Peng and Y. Li, *Nano Res.*, 2019, **12**, 1625-1630.

30 H. Wang, D. Yong, S. Chen, S. Jiang, X. Zhang, W. Shao, Q. Zhang, W. Yan, B. Pan and Y. Xie, *J. Am. Chem. Soc.*, 2018, **140**, 1760-1766.

31 H. Li, J. Shang, Z. Ai and L. Zhang, *J. Am. Chem. Soc.*, 2015, **137**, 6393-6399.

32 J. Wu, X. Li, W. Shi, P. Ling, Y. Sun, X. Jiao, S. Gao, L. Liang, J. Xu, W. Yan,

View Article Online
DOI: 10.1039/D0TA05733A

C. Wang and Y. Xie, *Angew. Chem. Int. Ed.*, 2018, **57**, 8719-8723.

33 R. Long, K. Mao, M. Gong, S. Zhou, J. Hu, M. Zhi, Y. You, S. Bai, J. Jiang, Q. Zhang, X. Wu and Y. Xiong, *Angew. Chem. Int. Ed.*, 2014, **53**, 3205-3209.

34 C. J. Wrasman, A. Boubnov, A. R. Riscoe, A. S. Hoffman, S. R. Bare and M. Cargnello, *J. Am. Chem. Soc.*, 2018, **140**, 12930-12939.

35 J. Di, J. X. Xia, S. Yin, H. Xu, L. Xu, Y. G. Xu, M. Q. He, H. M. Li and J. G. Wang, *Mater. Technol.*, 2015, **30**, 113-121.

36 X. Meng, Z. Li and Z. Zhang, *Mater. Res. Bull.*, 2018, **99**, 471-478.

37 X. Meng, Z. Li, J. Chen, H. Xie and Z. Zhang, *Appl. Surf. Sci.*, 2018, **433**, 76-87.

38 M. Pálmai, E. M. Zahran, S. Angaramo, S. Bálint, Z. Pászti, M. R. Knecht and L. G. Bachas, *J. Mater. Chem. A*, 2017, **5**, 529-534.

39 R. Wang, G. Qiu, Y. Xiao, X. Tao, W. Peng and B. Li, *J. Catal.*, 2019, **374**, 378-390.

40 H. Li, Y. Wu, C. Li, Y. Gong, L. Niu, X. Liu, Q. Jiang, C. Sun and S. Xu, *Appl. Catal. B: Environ.*, 2019, **251**, 305-312.

41 Y. Fang, T. Hua, W. Feng, D. M. Johnson and Y. Huang, *Catal. Commun.*, 2016, **80**, 15-19.

42 X. Shi, P. Wang, L. Wang, Y. Bai, H. Xie, Y. Zhou, J. A. Wang, Z. Li, L. Qu, M. Shi and L. Ye, *ACS Sustain. Chem. Eng.*, 2018, **6**, 13739-13746.

43 F. Raza, D. Yim, J. H. Park, H. I. Kim, S. J. Jeon and J. H. Kim, *J. Am. Chem. Soc.*, 2017, **139**, 14767-14774.

44 A. Lu, H. Sun, N. Zhang, L. Che, S. Shan, J. Luo, J. Zheng, L. Yang, D. L. Peng,

View Article Online
DOI: 10.1039/D0TA05733A

C. J. Zhong and B. Chen, *ACS Catal*., 2019, **9**, 7431-7442.

45 H. Yu, H. Huang, K. Xu, W. Hao, Y. Guo, S. Wang, X. Shen, S. Pan and Y. Zhang, *ACS Sustain. Chem. Eng*., 2017, **5**, 10499-10508.

46 S. Bai, X. Li, Q. Kong, R. Long, C. Wang, J. Jiang and Y. Xiong, *Adv. Mater*., 2015, **27**, 3444-3452.

47 X. Jin, C. Lv, X. Zhou, H. Xie, S. Sun, Y. Liu, Q. Meng and G. Chen, *Nano Energy*, 2019, **64**, 103955.

48 T. Li, Y. B. Li, X. C. Dai, M. H. Huang, Y. He, G. Xiao and F. X. Xiao, *J. Phy. Chem. C*, 2019, **123**, 4701-4714.

49 X. Chen, L. Liu, P. Y. Yu and S. S. Mao, *Science*, 2011, **331**, 746-750.

50 X. Xiong, L. Ding, Q. Wang, Y. Li, Q. Jiang and J. Hu, *Appl. Catal. B: Environ*., 2016, **188**, 283-291.

51 X. Wang, C. Liow, A. Bisht, X. Liu, T. C. Sum, X. Chen and S. Li, *Adv. Mater*., 2015, **27**, 2207-2214.

52 Y. Yan, Y. Yu, S. Huang, Y. Yang, X. Yang, S. Yin and Y. Cao, *J. Phys. Chem. C*, 2017, **121**, 1089-1098.

53 X. C. Dai, M. H. Huang, Y. B. Li, T. Li, B. B. Zhang, Y. He, G. Xiao and F. X. Xiao, *J. Mater. Chem. A*, 2019, **7**, 2741–2753.

54 R. Wang, B. Li, Y. Xiao, X. Tao, X. Su and X. Dong, *J. Catal*., 2018, **364**, 154-165.

55 X. Wu, Y. H. Ng, L. Wang, Y. Du, S. X. Dou, R. Amal and J. Scott, *J. Mater. Chem. A*, 2017, **5**, 8117-8124.

View Article Online
DOI: 10.1039/D0TA05733A

56 X. Song, J. Wang, R. Zhang, Y. Liu, G. Yu, Y. Dai, Z. Wang, P. Wang, Z. Zheng and B. Huang, *J. Phys. Chem. C*, 2019, **123**, 15599-15605.

57 K. Gelderman, L. Lee and S. W. Donne, *J. Chem. Educ*., 2007, **84**, 685-688.

58 S. W. LaGasse, P. Dhakras, K. Watanabe, T. Taniguchi and J. U. Lee, *Adv. Mater*., 2019, **31**, 1901392.

59 J. Guo, X. Liao, M. H. Lee, G. Hyett, C. C. Huang, D. W. Hewak, S. Mailis, W. Zhou and Z. Jiang, *Appl. Catal. B: Environ*., 2019, **243**, 502-512.

60 Y. Bai, H. Huang, C. M. Wang, R. Long and Y. J. Xiong, *Mater. Chem. Front.*, 2017, **1**, 1951-1964.

61 H. S. Su, H. S. Feng, Q. Q. Zhao, X. G. Zhang, J. J. Sun, Y. He, S. C. Huang, T. X. Huang, J. H. Zhong, D. Y. Wu and B. Ren, *J. Am. Chem. Soc*., 2020, **142**, 1341-1347.

62 F. Su, S. C. Mathew, G. Lipner, X. Fu, M. Antonietti, S. Blechert and X. Wang, *J. Am. Chem. Soc*., 2010, **132**, 16299-16301.

63 B. Zhang, X. Yang, J. Li and G. Cheng, *Chem. Commun*., 2018, **54**, 12194-12197.

64 H. Li, F. Qin, Z. Yang, X. Cui, J. Wang and L. Zhang, *J. Am. Chem. Soc*., 2017, **139**, 3513-3521.

65 C. Xu, Y. Pan, G. Wan, H. Liu, L. Wang, H. Zhou, S. H. Yu and H. L. Jiang, *J. Am. Chem. Soc*., 2019, **141**, 19110-19117.

66 G. Qiu, R. Wang, F. Han, X. Tao, Y. Xiao and B. Li, *Ind. Eng. Chem. Res*., 2019, **58**, 17389-17398.

67 Z. Guo, B. Liu, Q. Zhang, W. Deng, Y. Wang and Y. Yang, *Chem. Soc. Rev.*,

2014, **43**, 3480-3524.

68 Y. Nosaka and A. Y. Nosaka, *Chem. Rev.*, 2017, **117**, 11302-11336.

69 Y. Z. Chen, Z. U. Wang, H. Wang, J. Lu, S. H. Yu and H. L. Jiang, *J. Am. Chem. Soc.*, 2017, **139**, 2035-2044.

70 H. Wang, S. Chen, D. Yong, X. Zhang, S. Li, W. Shao, X. Sun, B. Pan and Y. Xie, *J. Am. Chem. Soc.*, 2017, **139**, 4737-4742.

71 X. Sun, X. Luo, X. Zhang, J. Xie, S. Jin, H. Wang, X. Zheng, X. Wu and Y. Xie, *J. Am. Chem. Soc.*, 2019, **141**, 3797-3801.

72 T. Wang, X. Tao, Y. Xiao, G. Qiu, Y. Yang and B. Li, *Catal. Sci. Technol.*, 2020, **10**, 138-146.

73 A. M. Robinson, L. Mark, M. J. Rasmussen, J. E. Hensley and J. W. Medlin, *J. Phys. Chem. C*, 2016, **120**, 26824-26833.

74 R. Long, K. Mao, X. Ye, W. Yan, Y. Huang, J. Wang, Y. Fu, X. Wang, X. Wu, Y. Xie and Y. Xiong, *J. Am. Chem. Soc.*, 2013, **135**, 3200-3207.

75 J. Al-Nu'airat, M. Altarawneh, I. Oluwoye, X. Gao and B. Z. Dlugogorski, *Energy Fuels*, 2018, **32**, 12851-12860.

View Article Online
DOI: 10.1039/D0TA05733A

Figures and Captions

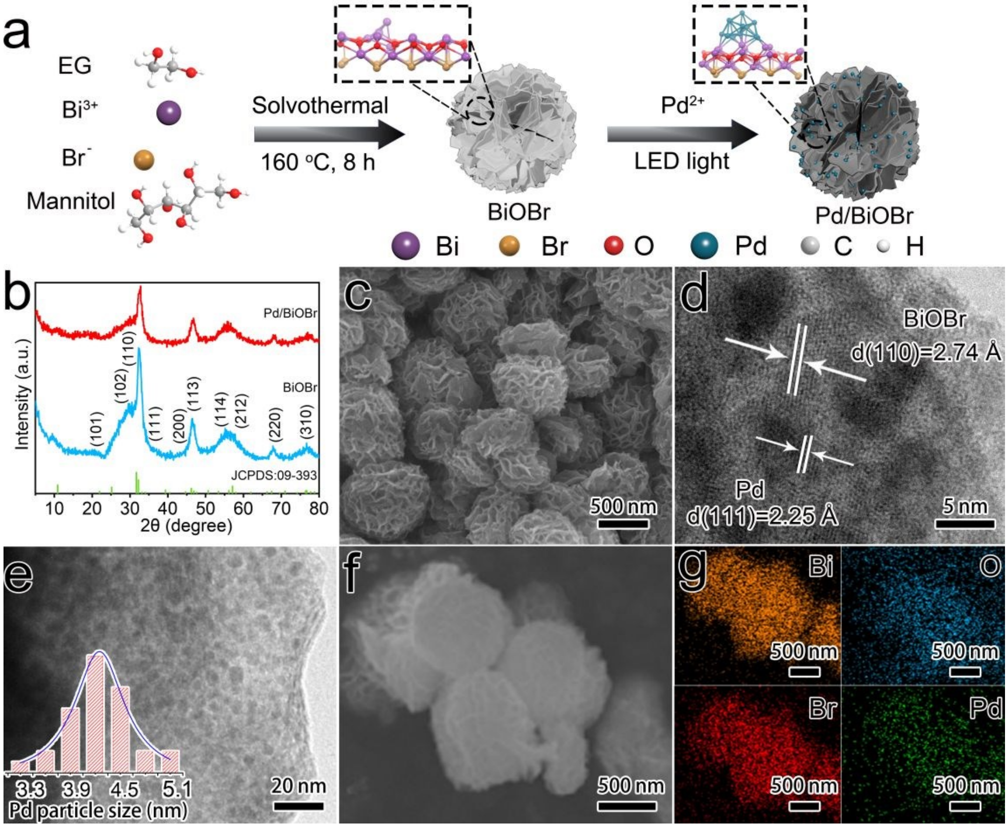

Fig. 1 (a) Schematic illustration for the synthesis of Pd/BiOBr photocatalyst, (b) XRD patterns of BiOBr and Pd/BiOBr samples. (c) SEM image, (d) HRTEM image, (e) TEM image (inset: size distribution of Pd NPs), (f) SEM imaging and (g) the corresponding elemental mappings of Pd/BiOBr sample.

DOI: 10.1039/D0TA05733A

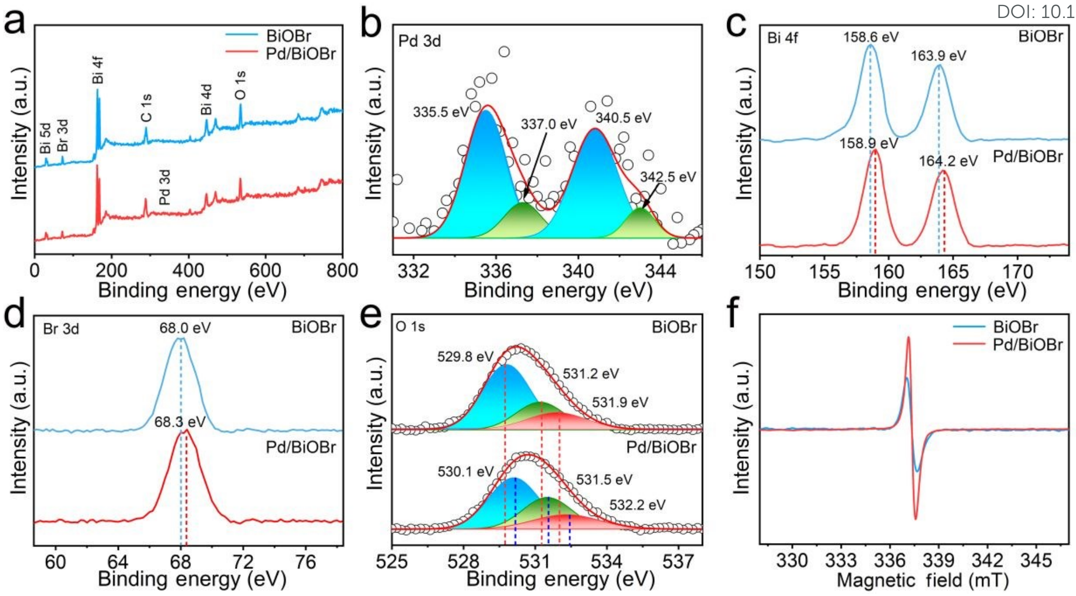

Fig. 2 (a-e) XPS spectra and (f) ESR spectra of BiOBr and Pd/BiOBr samples.

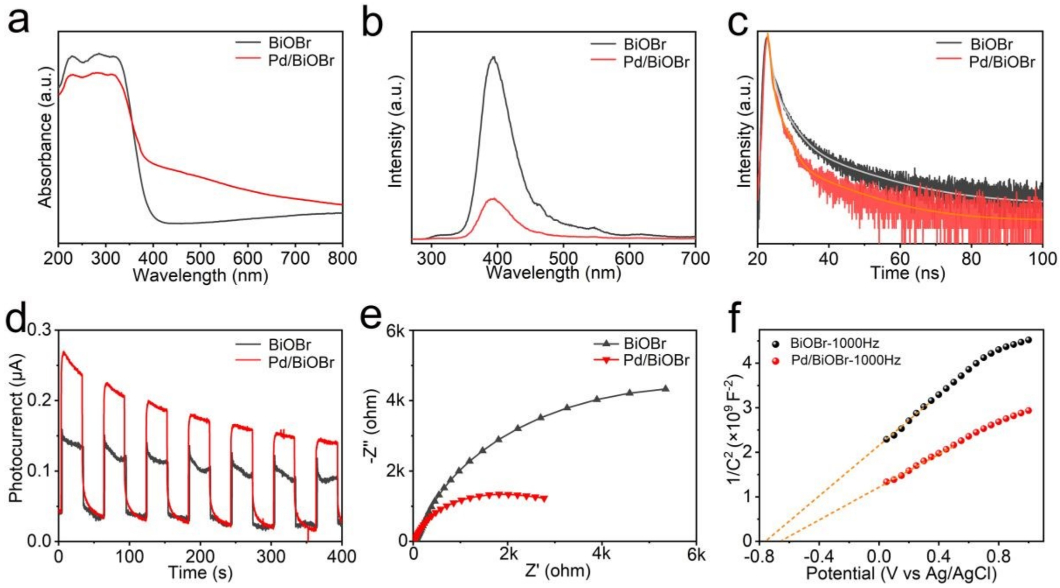

Fig. 3 (a) UV-vis DRS spectra, (b) room-temperature PL spectra, (c) TRPL decay curves, (d) transient photocurrent responses, (e) EIS Nyquist plots and (f) M-S plots of BiOBr and Pd/BiOBr samples.

View Article Online
DOI: 10.1039/D0TA05733A

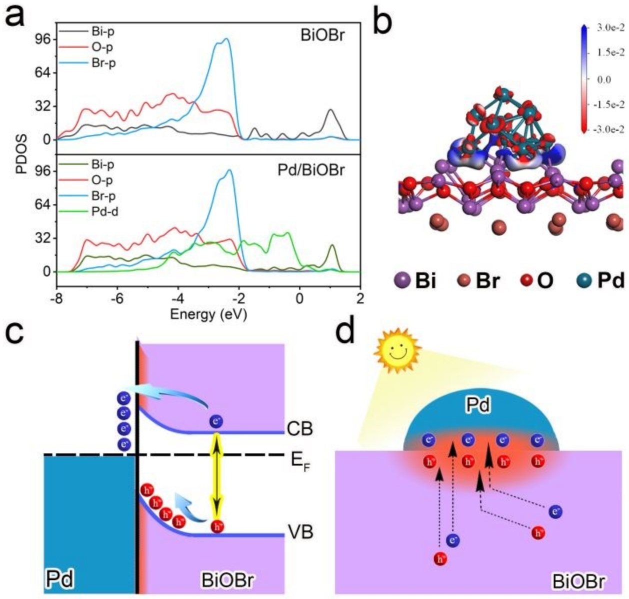

Fig. 4 (a) PDOS plots of BiOBr-V_O with and without Pd cluster, (b) charge density difference of Pd/BiOBr-V_O (001), where blue denotes electron accumulation and red represents electron depletion. (c) Illustration of the photoexcited charge transfer at Pd-BiOBr interface with a Schottky barrier. (d) Illustration of the photogenerated electron-hole migration and separation at Pd-BiOBr interface.

View Article Online
DOI: 10.1039/D0TA05733A

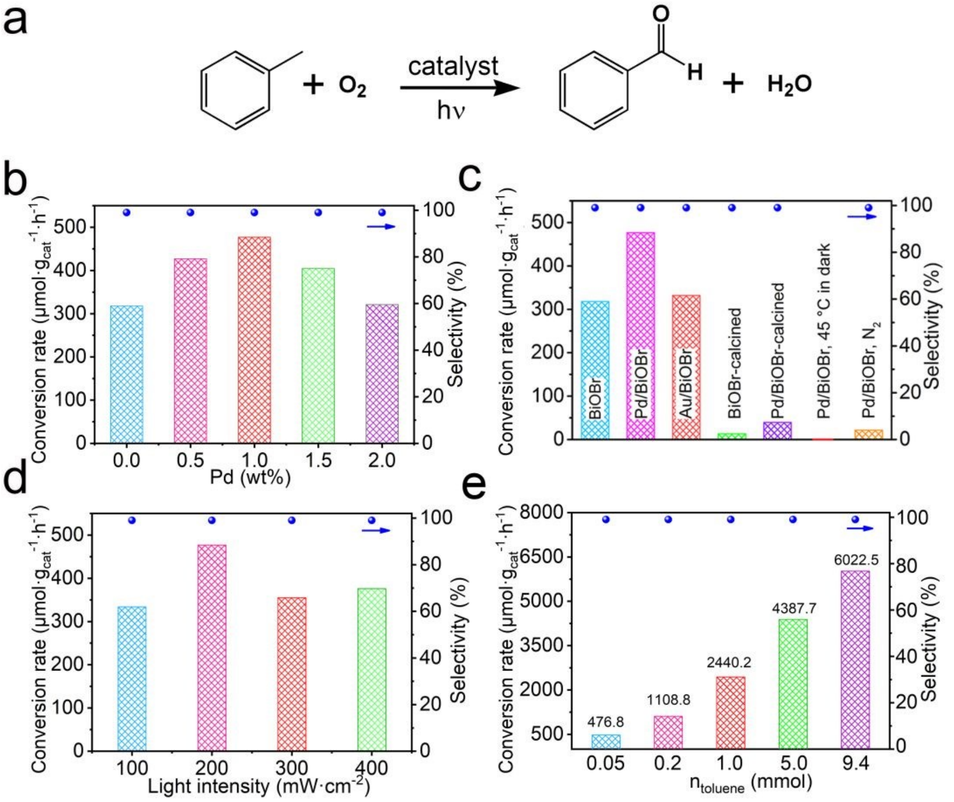

Fig. 5 The photocatalytic selective oxidation of toluene to benzaldehyde. (a) The photocatalytic reaction, (b) the results from Pd(*x*)/BiOBr photocatalysts with different Pd loading contents, (c) the results from different photocatalysts or reactions under different conditions, (d) the results from the Pd/BiOBr photocatalyst under the UV-visible irradiation of different optical power densities, (e) the results from the Pd/BiOBr photocatalyst with different dosages of toluene.

View Article Online
DOI: 10.1039/D0TA05733A

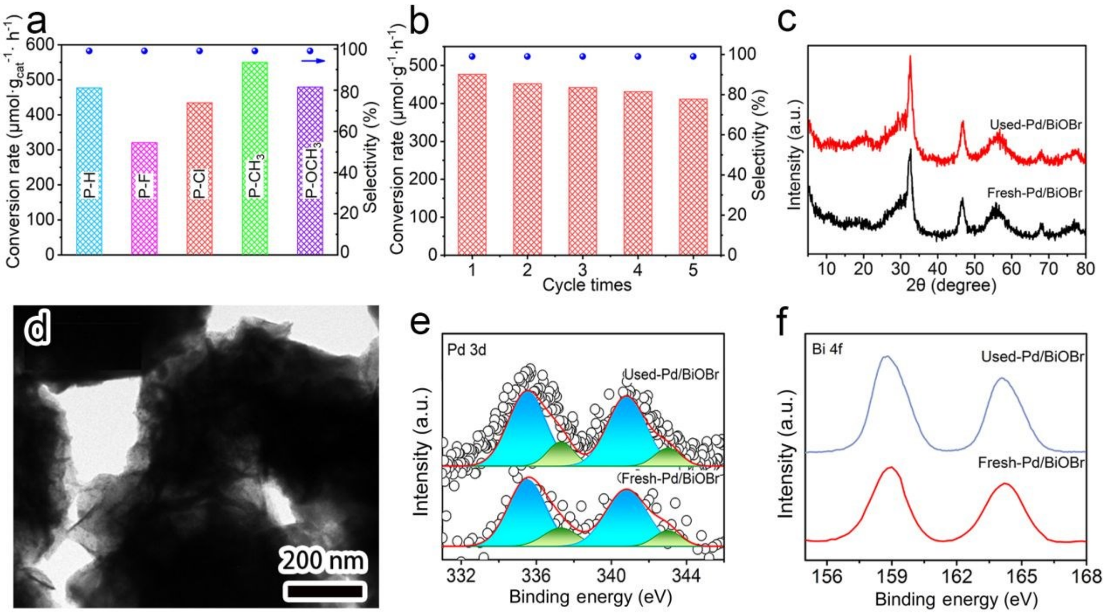

Fig. 6 (a) Photocatalytic selective oxidation of various toluene derivatives over Pd/BiOBr catalyst after 5 h, (b) five catalytic cycles of photocatalytic selective oxidation of toluene over Pd/BiOBr catalyst, (c) XRD patterns of the fresh and used Pd/BiOBr photocatalysts, (d) TEM image of the used Pd/BiOBr photocatalyst, (e) Pd 3d and (f) Bi 4f XPS spectra of the used Pd/BiOBr photocatalyst.

View Article Online
DOI: 10.1039/D0TA05733A

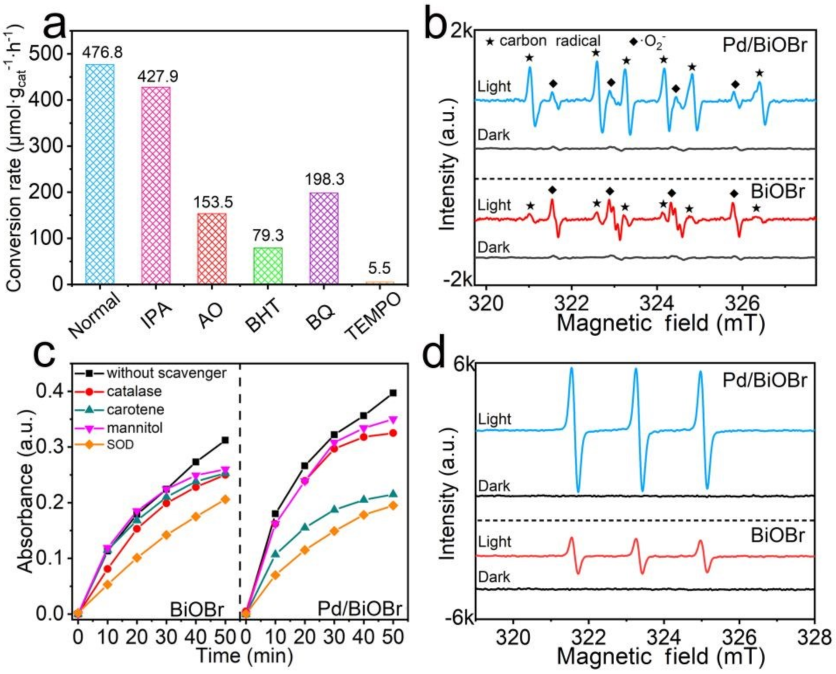

Fig. 7 (a) Photocatalytic toluene conversion over Pd/BiOBr with adding different scavengers after 5 h irradiation, (b) *in-situ* ESR detection of radicals with adding DMPO in the photocatalytic toluene oxidation, (c) the absorbance evolution of TMB oxidation monitored at the 370 nm peak in the presence of different scavengers, (d) *in-situ* ESR detection of $^1O_2$ with adding TEMP in photocatalytic toluene oxidation.

View Article Online
DOI: 10.1039/D0TA05733A

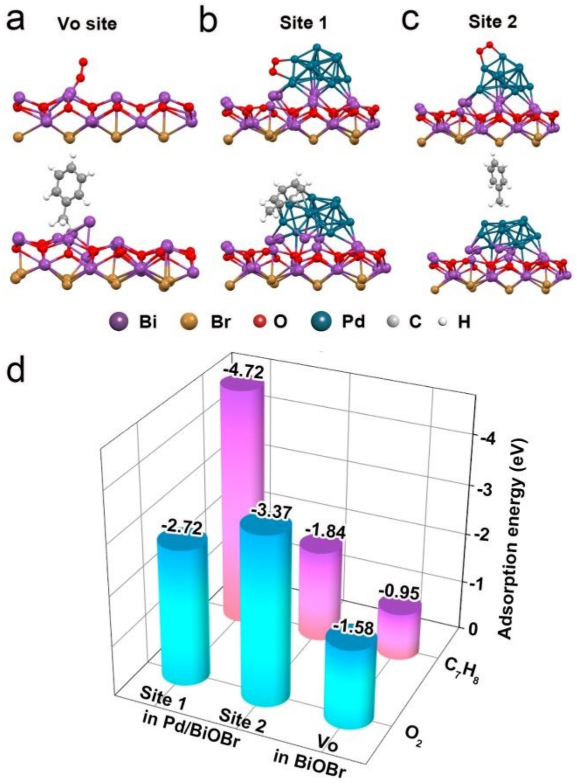

Fig. 8 DFT-calculated local configurations for O_2 and toluene adsorbed onto (a) V_O site in BiOBr-V_O surface, (b) interfacial Pd site (Site 1) and (c) top Pd site (Site 2) in Pd/BiOBr-V_O surface. (d) The adsorption energies (E_{ad}) for O_2 and toluene absorbed onto the different sites.

View Article Online
DOI: 10.1039/D0TA05733A

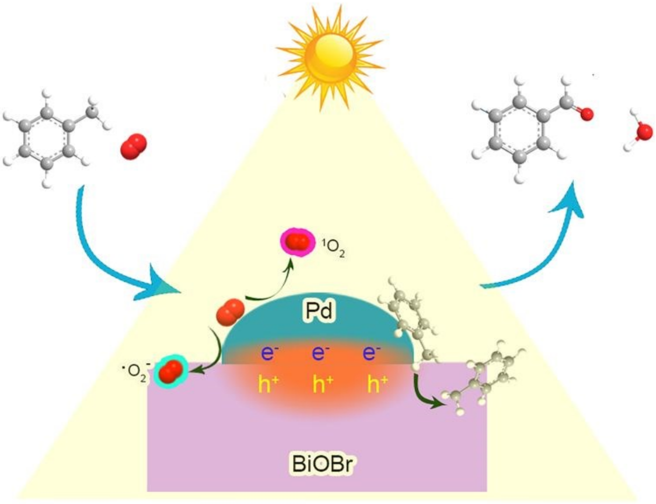

Fig. 9. Proposed mechanism of photocatalytic selective toluene oxidation to benzaldehyde over Pd/BiOBr catalyst.

View Article Online
DOI: 10.1039/D0TA05733A

Table of Contents

The enhanced charge separation and molecule activation at Pd-BiOBr interface greatly promote the photocatalytic selective oxidation of toluene to benzaldehyde.